# Long-term Study of the Solar Filaments from the Synoptic Maps as Derived from $H_\alpha$ Spectroheliograms of the Kodaikanal Observatory

Subhamoy Chatterjee[1] , Manjunath Hegde[1], Dipankar Banerjee[1,2] , and B. Ravindra[1]
[1] Indian Institute of Astrophysics, Koramangala, Bangalore 560034, India; dipu@iiap.res.in
[2] Center of Excellence in Space Sciences India, IISER Kolkata, Mohanpur 741246, West Bengal, India

## Abstract

The century long (1914–2007) $H_\alpha$ (656.28 nm) spectroheliograms from the Kodaikanal Solar Observatory (KSO) have been recently digitized. Using these newly calibrated, processed images we study the evolution of dark elongated on-disk structures called filaments, which are potential representatives of magnetic activities on the Sun. To our knowledge, this is the oldest uniform digitized data set with daily images available today in $H_\alpha$. We generate Carrington maps for the entire time duration and try to find the correlations with maps of the same Carrington rotation from the Ca II K KSO data. Filaments are segmented from the Carrington maps using a semi-automated technique and are studied individually to extract their centroids and tilts. We plot the time-latitude distribution of the filament centroids, producing a butterfly diagram which clearly shows the presence of poleward migration. We separate polar filaments for each cycle and try to estimate the delay between the polar filament number cycle and the sunspot number cycle peaks. We correlate this delay with the delay between polar reversal and sunspot number maxima. This provides new insight on the role of polar filaments on polar reversal.

*Key words:* methods: data analysis – Sun: chromosphere – Sun: filaments, prominences – techniques: image processing

*Supporting material:* tar.gz file

## 1. Introduction

The Sun is a star that is highly heterogeneous, both temporally and spatially. It is crucial to study the long-term evolution of the magnetic field, which is believed to be the major driver for this heterogeneity. Before the 1970s, regular magnetic field measurements were not available and thus the long-term study of proxies of solar magnetic field has been an important subject area. Solar filaments have served as one such proxy (McIntosh 1972) for understanding the magnetic activity of the Sun. They are clouds of ionized gas projected against the solar disk that are cooler and denser than the plasma underneath. In $H_\alpha$ ($\approx$656.28 nm line center) observations they appear as dark, elongated, thin, hairy structures. Filaments are formed along the polarity inversion line between opposite magnetic polarities (Martin 1998). When a filament becomes unstable due to magnetohydrodynamic instability, it erupts. Filament eruption is often associated with flare and coronal mass ejections (CMEs), which are sources of geomagnetic storms (Gilbert et al. 2000; Gopalswamy et al. 2000, 2003; Chen et al. 2008; Zhang et al. 2012).

Solar filaments are seen at all latitudes on the solar disk from equator to pole during all phases of the solar cycle, and outline the boundary between different magnetic field polarities. This makes them ideal candidates for the study of large-scale concentrations of weaker magnetic fields on the Sun (McIntosh 1972; Low 1982; Makarov & Sivaraman 1983). Thus, long-term filament data can be efficiently used as a proxy for magnetic activity of the Sun. Additionally, the study of the occurrence of filaments provides useful insight into the distribution of these fields on the solar surface, and their evolution, and help in the understanding of the nature of the Sun's magnetic field (Mouradian & Soru-Escaut 1994). The detection of filaments from the archival images is the first step for such a study. There have been many attempts to detect

filaments in an automated way from full-disk $H_\alpha$ images. The methods range from modified Otsu thresholding (Hao et al. 2015) to the application of artificial neural networks (Zharkova & Schetinin 2003). But most of these methods were applied only on good-quality digital images of a few recent solar cycles. Historical digitized data contains many inherent artifacts that can not be corrected by flat fielding (Zharkova et al. 2005). The application of the majority of automated methods on such data mostly results in an under-estimation or over-detection of filaments. So a careful detection of such features is necessary and may require manual intervention. The detection of filaments from Carrington/synoptic maps of historical data has generated promising results, as reported by a few recent studies. Li et al. (2007) used synoptic charts of the filament archive from the Meudon observatory to study the long-term variation of solar filaments. Using the same data set, Li (2010) studied the latitude migration of filaments at low latitudes (less than 50°), and found that the latitudinal drift of filaments differs from those of sunspot groups. Hao et al. (2015) utilized the Big Bear Solar Observatory (BBSO) data from 1988–2013 to extract variation of filament area, spine length, tilt angle, and barb number with respect to the calendar year and latitude. The study also included the north–south asymmetry of the filament number. Tlatov et al. (2016a, 2016b), using synoptic charts from the Meudon Observatory and Kislovodsk Mountain Astronomical Station, studied the variation of the filament tilt angle and classified filaments with different tilt angle, namely, active region filaments, quiescent filaments, and polar filaments. Some studies have utilized the Kodaikanal historical data on prominences (Ananthakrishnan 1952; Evershed 1907, 1908; Rausaria et al. 1993a) and flares (Rausaria et al. 1993b; Sundara Raman et al. 1994, 2001). Most of these earlier studies were for a shorter period of time. Ananthakrishnan (1952) used Ca II K disk blocked plates to study the evolution of prominences until 1950,
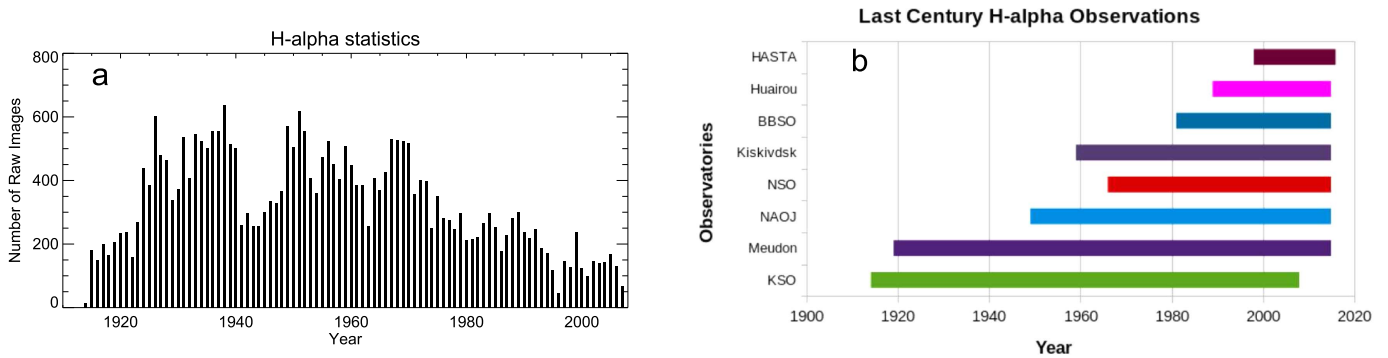
**Figure 1.** Availability of H$_\alpha$ images. (a) Yearly histogram of KSO H$_\alpha$ data and (b) the availability of the H$_\alpha$ data set across the globe. Different sources are marked with abbreviations along the y-axis.

and Makarov & Sivaraman (1983) used Kodaikanal Ca II K and H$_\alpha$ plates until 1919 to study the poleward migration of magnetic neutral lines. In this paper, we present for the first time the newly digitized unique data set of H$_\alpha$ filaments from the Kodaikanal Solar Observatory (KSO) and study the solar activity variation for nine solar cycles. To our knowledge, this is the oldest digitized archive of H$_\alpha$. In Section 2, we present the description of the data. The methods of our analysis, and the representative results are presented in Sections 3 and 4, respectively. Finally, in Section 5 we summarize our results and discuss the potential of such a unique archive for future studies.

## 2. Data Description

Systematic H$_\alpha$ observations have been carried out at KSO since 1914 with a telescope (spectroheliograph) with a 30 cm objective and an f-ratio of 21. The spectroheliograms (656.3 nm) were consistently recorded in photographic plates until 1978, and subsequently in films on a daily basis. These plates/films have recently been digitized with the help of a uniform illumination source and a $4096 \times 4096$ CCD cooled at $-100\,°C$. We used the digitized full disk $4096 \times 4096$ KSO H$_\alpha$ density images from 1914 to 2007 ($\approx 0.86$ arcsec/pixel) in our current study. The seeing-limited resolution has been $\approx 2$ arcsec for the majority of the observing period. Figure 1(a) shows the number of images available in the archive (used in this paper) and Figure 1(b) shows the time span over which the KSO digitized images are available, along with other major data sources. The observation for the time duration close to that of Kodaikanal has been provided by the Meudon Observatory, France (since 1919; Figure 1(b)). Recent studies with this data have been performed by Tlatov et al. (2016a, 2016b), combined with the H$_\alpha$ observations of the Kislovodsk Mountain Astronomical Station, Pulkovo Astronomical Observatory, the Russian Academy of Sciences after 1959.

## 3. Methods

### 3.1. Calibration

The calibration includes several steps. First the RAW (digitized and uncalibrated) images (Figure 2(a)) were inverted in grayscale. Edge detection operators were applied to produce a binary edge detected image. The Circle Hough Transform (Sonka et al. 2014) technique was applied on that binary image to find the center and radius of the disk. After centering the disk, the images were resized to a smaller version and were median-filtered to obtain the asymmetric limb-darkening

profile, combining the effects of the line-of-sight and the imaging instrument. This step was applied to reduce the time complexity of the automated calibration per image as the limb-darkening profile captures only the large-scale intensity variation. The profile was again blown up to its original size and the original image was divided to generate limb-darkening corrected images, as shown in Figure 2(b).

### 3.2. Carrington Map Generation

A Carrington map is a type of Mercator projection of the spherical Sun generated from synoptic observations corresponding to one solar rotation. In this study, 60° longitude bands ($-30°$ to 30° heliographic longitude) in the limb-darkening corrected full-disk H$_\alpha$ images were selected. These were $B_0$-angle corrected and mapped to the Carrington longitude-latitude grid in the form of a rectangle with a weightage of cosine 4th power (Sheeley et al. 2011) over each heliographic longitude. These rectangular slices were shifted and added according to the date and time for 27.2753 days to generate a full 360-degree map of the Sun. A similar 360-degree map was obtained from rectangular binary slices called a streak map (Sheeley et al. 2011; Chatterjee et al. 2016). The overlap of the same Carrington longitudes was removed through the division of the original solar 360-degree map with the streak map to form an image called a Carrington, or Synoptic, map. One representative Carrington map is shown in Figure 2(c). A total of 1215 Carrington maps from rotations 817 to 2062 are posted on this portal (ftp://ftp.iiap.res.in/subhamoy/halpha_carrington_maps_kodaikanal/) and are available in a tar.gz archive. Figure 3 depicts three representative Carrington maps for three different phases of the solar cycles. Figures 3(a)–(c) present, respectively, the rising phase, the maxima of cycle 16, and the minima of cycle 20. It can be observed from the maps that polar filaments are dominantly present during the rising phase and minima of the solar cycles, whereas low-latitude filaments dominantly occur in between, i.e., around cycle maxima. It should be noted that bright and dark ridge-like structures in the Carrington maps are not of solar origin. Scratch lines present in the RAW images are responsible for those and they manifest as a curved shape in the Carrington maps due to the north–south rotation correction.

### 3.3. Filament Detection and Parameter Extraction

Figure 4(a) shows the Carrington rotation 1823 with many filaments and an artifact mimicking a filament marked with a red arrow. If a fully automated filament detection algorithm is
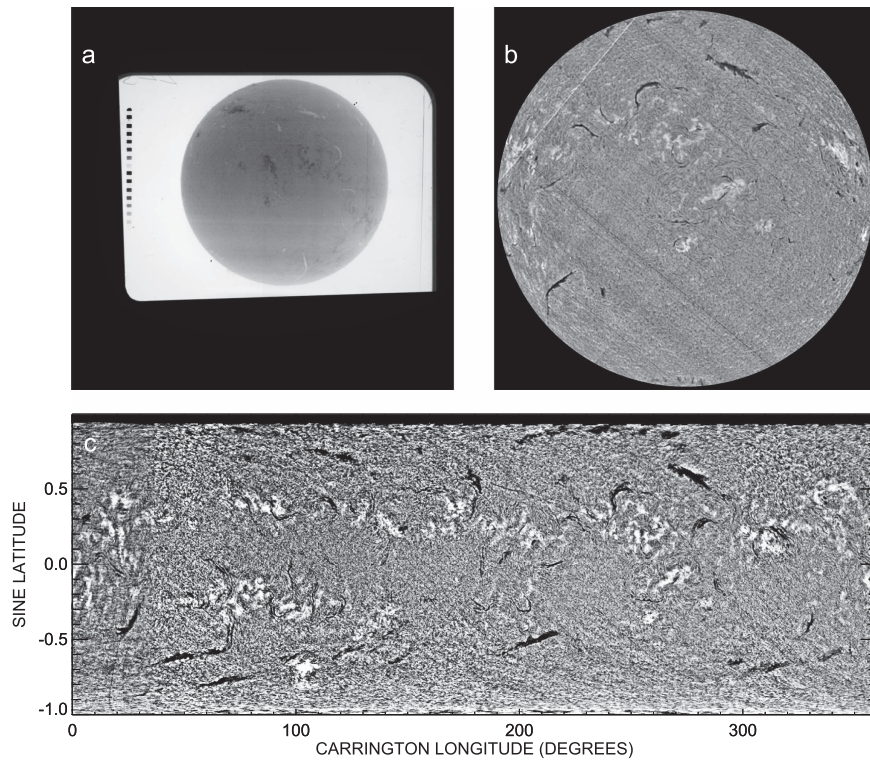
**Figure 2.** KSO H$_\alpha$ data calibration and filament detection. (a) H$_\alpha$ RAW image taken on 1981 March 16, (b) a limb-darkening corrected and disk-centered image, and (c) a Carrington map for rotation number 1706 starting on 1981 March 8.
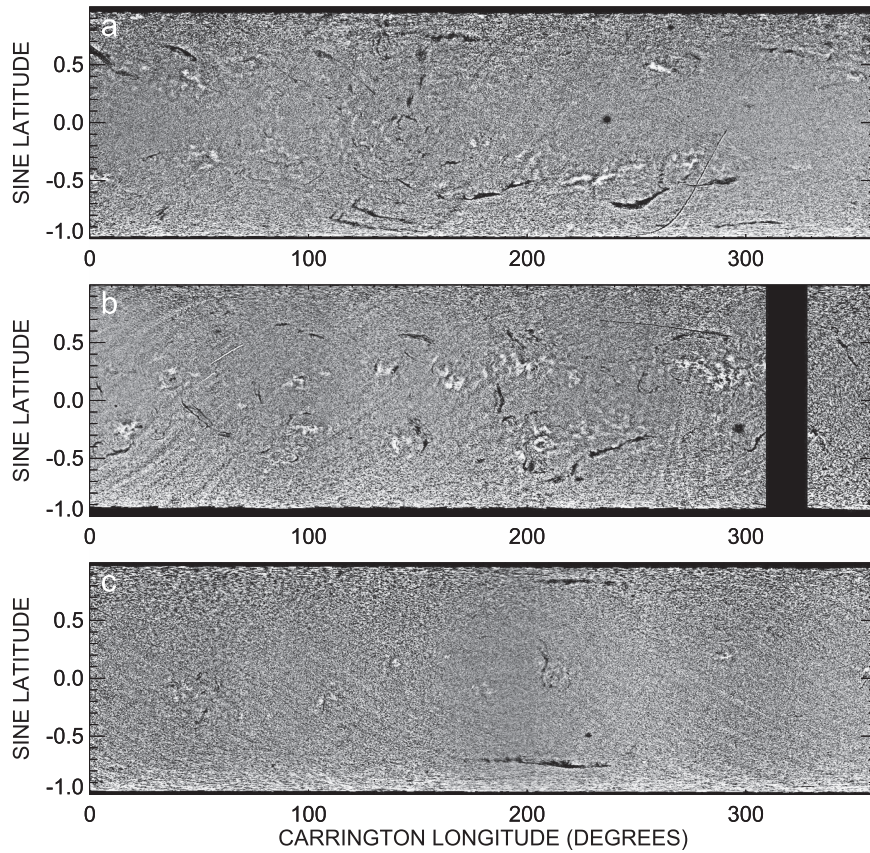


**Figure 3.** KSO H$_\alpha$ maps for different phases of the solar cycles. (a) Carrington rotation 970, depicting a representative filament distribution at the rising phase of cycle 16, (b) Carrington rotation 1001, depicting a representative filament distribution at the maxima of cycle 16, and (c) Carrington rotation 1641, depicting a representative filament distribution at the minima of cycle 20.
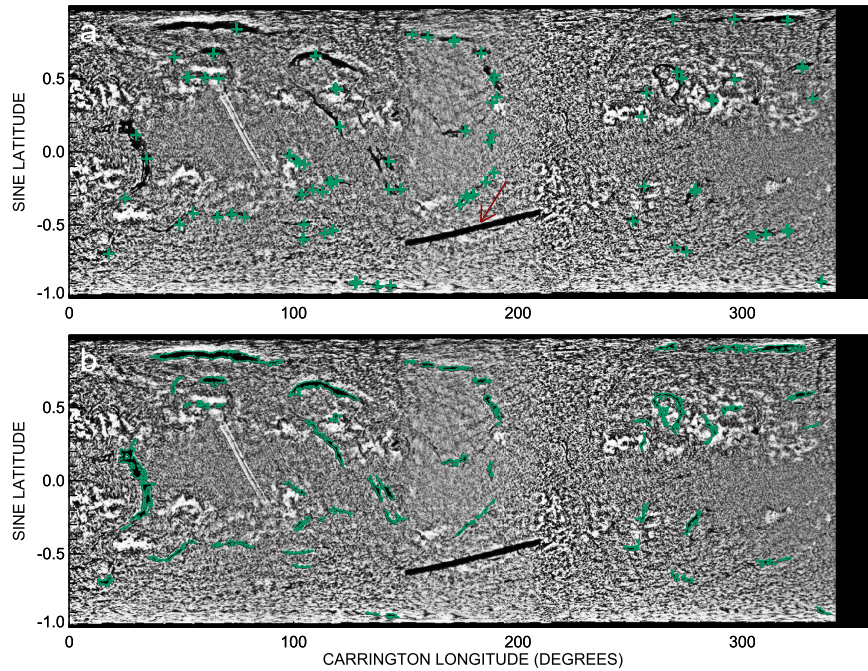
**Figure 4.** Region growing for KSO H$_\alpha$ filament detection. (a) H$_\alpha$ Carrington rotation 1823 with seed points marked with green "+" symbols. The scratch line resembling a filament is marked with red arrow and (b) the green contours depict the filament boundaries detected through region growing about the manually selected contours.

used, the artifact will be detected as a filament. This was the reason we chose the semi-automated technique. The Carrington maps were first intensity enhanced through histogram equalization. Seed points (shown with "+" in Figure 4) were selected manually on the dark filaments. In order to detect a filament for each selected seed point, the eight-neighborhood region growing method (Bonnin et al. 2013; Sonka et al. 2014) was used. A similar method for filament extraction from full-disk Meudon data of the year 2002 has been used by Bonnin et al. (2013). The region grows by including neighbor pixels around the seed point, satisfying the intensity threshold. This process is repeated for each new neighbor pixel until the pixels extend totally outside the intensity threshold and a connected region is produced. As we see in Figure 4(a), some of the filaments need multiple seed-point selection for sudden jumps of intensity above the threshold selected for growing the region. Subsequently, binary-filament-detected Carrington maps are generated. The contour of the produced binary map for rotation 1823 is overplotted in green on the grayscale Carrington map in Figure 4(b). Because of the image contrast, data gaps, and temporal evolution, naturally the Carrington maps depict unnatural fragmentation in the filaments. As the length of the polar filaments (latitude $>50°$) increases, the effect upon them also increases. Morphological closing operations with different kernel sizes are performed for higher-latitude filaments in order to examine the change in the number of polar filaments. Parameters such as centroid longitude, latitude, and filament tilts are generated. In Figure 5(a) we show the Ca II K Carrington map as generated from the KSO data in order to compare the correspondence between the bright plage locations in Ca II K (Figure 5(a)) and their traces in H$_\alpha$ (Figure 5(b)), corresponding to the rotation 1706. To make correlations between filaments and active regions more evident, we plotted the filament skeletons on the Ca II K as shown in Figure 5(c). we generated Carrington maps using the Michelson Doppler Imager (MDI) on-board SoHO

line-of-sight magnetograms available after the year 1996, and Figure 6 includes an MDI map for the inspection of the location of filaments in terms of the distribution of the magnetic fields. Carrington rotation 1962 has been compared with Ca II K, H$_\alpha$, and MDI in Figures 6(a)–(c), respectively. The formation of filaments along magnetic neutral lines can be observed at different locations, and one such example is shown in the zoomed inset of Figure 6(d).

## 4. Results

Figure 7(a) shows the temporal evolution of the filament centroid latitudes over nine cycles. This plot illustrates how the filaments are distributed at all latitudes and also reveals (like sunspots) that filaments also migrate toward the equator (butterfly diagram) but from a higher latitude. Along with the butterfly diagram-like nature, a signature of the poleward migration is observed in the plot. One such example is highlighted by a red circle with an arrow. Corresponding to cycles 15, 17, 20, 21, and 23 in the southern hemisphere, a rush to the pole is clearly seen. Similarly, in the northern hemisphere, cycles 15,16, 20, 21, and 23 show this behavior. Though there are traces, poleward rush is not very clear for cycles 18, 19, and 22. The observed polar rush can be compared with the same from the Ca II K prominence results as presented in Ananthakrishnan (1952). Though we do not observe the rush until pole because of the projection effects on the on-disk feature, we find the early phases for most of the cycles. Now we focus our attention to the polar filaments. Figure 7(b) shows the temporal variation of the number of polar filaments (centroid latitude $>50°$) overplotted on the smoothed sunspot number (SSN) from the Solar Influences Data Center (SIDC; http://www.sidc.be/silso/datafiles). We must note that we find some cases of fragmentation in the filaments during the detection and, at this point, we do not have a method to estimate the correct length for such cases.
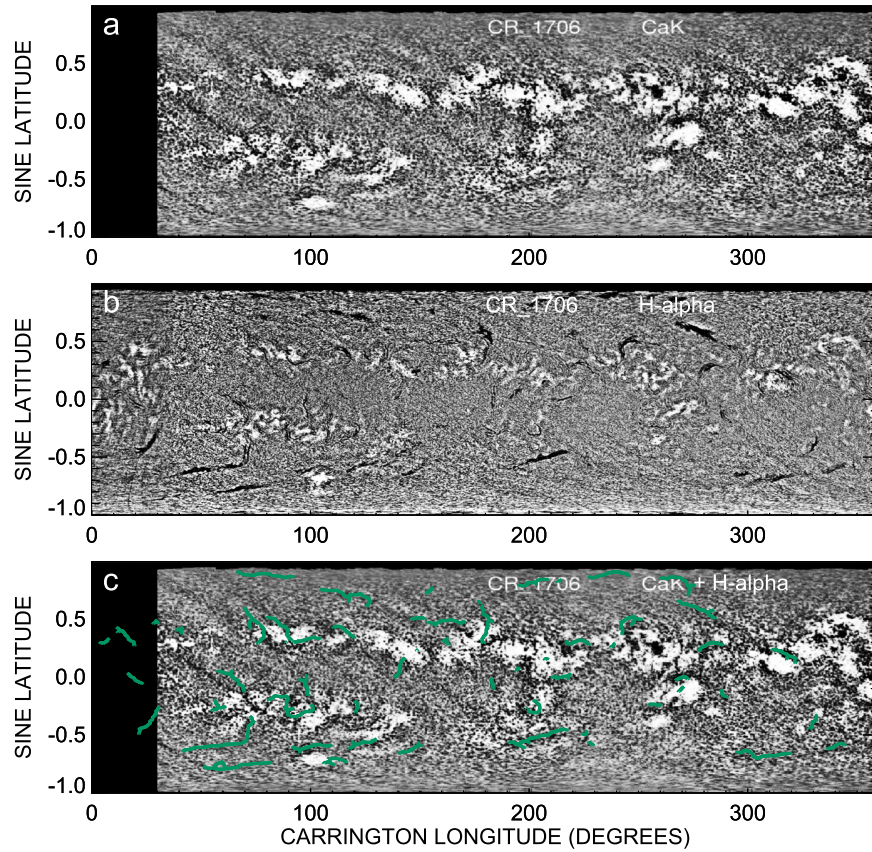
**Figure 5.** Correlation between KSO Ca II K and Hα maps. (a) KSO Ca II K Carrington rotation 1706, (b) KSO Hα Carrington rotation 1706, and (c) the filament spine in green from (b) overplotted on (a).

Thus we concentrate on the number density of the filaments rather than the exact length estimates. We apply Morph close operations on the detected filaments with disk kernels of a radii of 22 and 30 pixels named as kernel 1 and kernel 2, respectively, in Figure 7(b). The target Carrington maps are $1570(x) \times 500(y)$ in size with the $x$-axis (or longitude) spanning from 0° to 360° and the $y$-axis (or sine latitude) spanning over −1 to 1. In this exercise we explore whether the temporal location of the polar filament number maxima changes with the variation of the kernel sizes. Figure 7(b) illustrates the natural reduction of the filament number with a higher kernel size, though there is no apparent change in the epoch of the maxima. Both of the time series clearly present 11-year periodicity with same delay between their peaks and SSN maxima. Based on the Wilcox Solar Observatory polar field data (taken from http://wso.stanford.edu/), we plot the SSN-polar filament maxima delay versus the SSN maxima-pole reversal delay in Figure 8 from three cycles, namely 21, 22, and 23. To understand the epoch of pole reversal the (north–south)/2 curve is considered. They show a linear correlation ($r$) of 0.99. As the number of data points are limited, we also calculate the Adjusted Pearson Correlation Coefficient defined by the expression

$$r^2_{\mathrm{adjusted}} = 1 - (1 - r^2) \frac{n - 1}{n - p - 1},$$

where $n$ is the number of data points, which is three in our case, and $p$ is the number of independent variables, which here is one. We find the adjusted coefficient to be 0.98, which remains

relatively high, confirming the association between the epoch of the number of polar filament peak and pole reversal with respect to the sunspot maxima. This emphasizes the role of the polar filaments in polarity reversals. The faster the polar filaments migrate to poles, the earlier the pole reversal will be. In our understanding this is a very important finding and demands a detailed study, which we plan to do in the near future.

Now we will look at the tilt angle distribution. Figure 9(a) illustrates a histogram of the solar filament tilt angle with respect to the equator. It shows an asymmetric nature consistent with the findings of Tlatov et al. (2016b). We also take the average of the tilt angle absolute values for different latitude bands. This latitudinal distribution is plotted in Figure 9(b). It is consistent with the Joy's law for sunspot pairs. Though we do not estimate the exact length of the filaments, we believe that the average tilt of the fragmented filaments (a fraction of the total sample) are more or less the same as that of the fitted straight line slope of the whole filament; thus, this plot should not change much due to filament fragmentation. As the filaments are expected to be oriented along neutral lines, they become more parallel to the equator at higher latitudes where the sunspot pairs (appearing till ≈40°) become more tilted. It is worth mentioning that filaments appear all over the disk, reaching much higher latitudes compared to those of the sunspot pairs, and they maintain the trend of a declining tilt with respect to the equator. Thus the filament distribution may provide a detailed insight into the distribution of the magnetic field at all latitudes, rather than the sunspot locations alone.
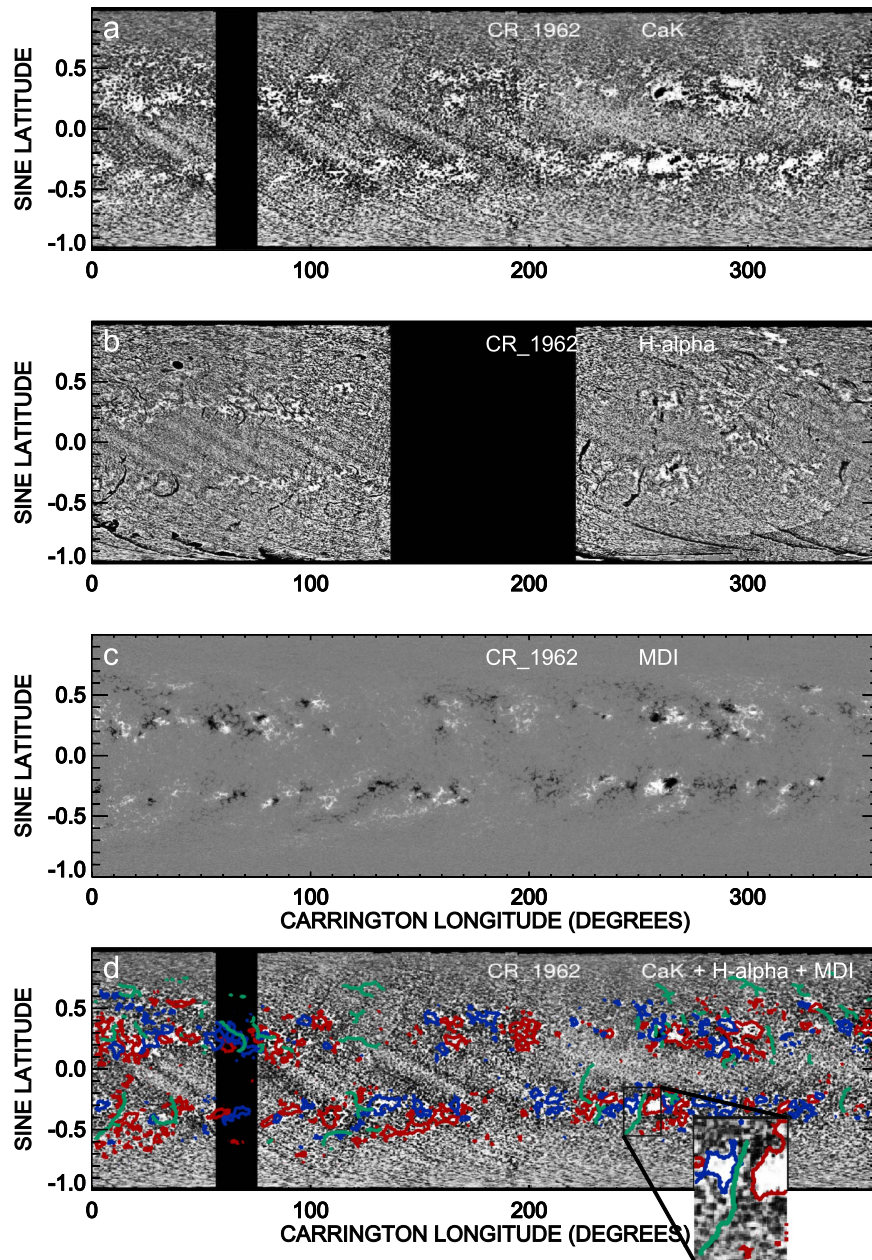
**Figure 6.** Correlation between KSO Ca II K, H$_\alpha$, and MDI magnetogram maps. (a) KSO Ca II K Carrington rotation 1962, (b) KSO H$_\alpha$ Carrington rotation 1706, (c) Carrington map generated from MDI/SoHO full-disk LOS magnetograms for rotation 1962, and (d) the filament spine in green from (b) overplotted on (a) with positive (red) and negative (blue) magnetic field contours of rotation 1962 from MDI/SoHO. This panel also shows a magnified view of a small window within the Carrington map depicting a filament lying in between two magnetic patches of opposite polarity.

## 5. Conclusions

In this paper, we present the calibration (no density-to-intensity calibration has been performed yet) and processing of the RAW H$_\alpha$ data set (1914–2007) from KSO. We have generated Carrington maps from the calibrated and processed daily spectroheliograms for the whole study period. To our knowledge, for the first time we have been able to produce Carrington maps of H$_\alpha$, spanning almost 100 years, from digitized images taken from a single observatory. This could be the most uniform and longest database for the statistical studies on H$_\alpha$. A semi-automated algorithm relying on seed selection and region growing has been used to consistently detect filaments from the Carrington maps. From the detected maps we have generated parameters such as filament centroid latitude and tilt angle with respect to the equator. Salient features of the new findings are listed here.

1. We have generated the time-latitude distribution of filaments, giving a clear signature of polar rush for several cycles along with a butterfly diagram-like pattern. It is worth noting that Cycle 23 shows a comparable signature to that of polar rush as presented in Figure 5 of Hao et al. (2015).
2. We segregated polar filaments with a centroid latitude greater than $50°$ and plotted their number for all the Carrington maps over time. The plot depicted a similar 11-year periodicity as normally observed for a sunspot number cycle with delays. We measured the delays between polar filament and sunspot number maxima. We also utilized the epochs of the polar magnetic field reversal from the
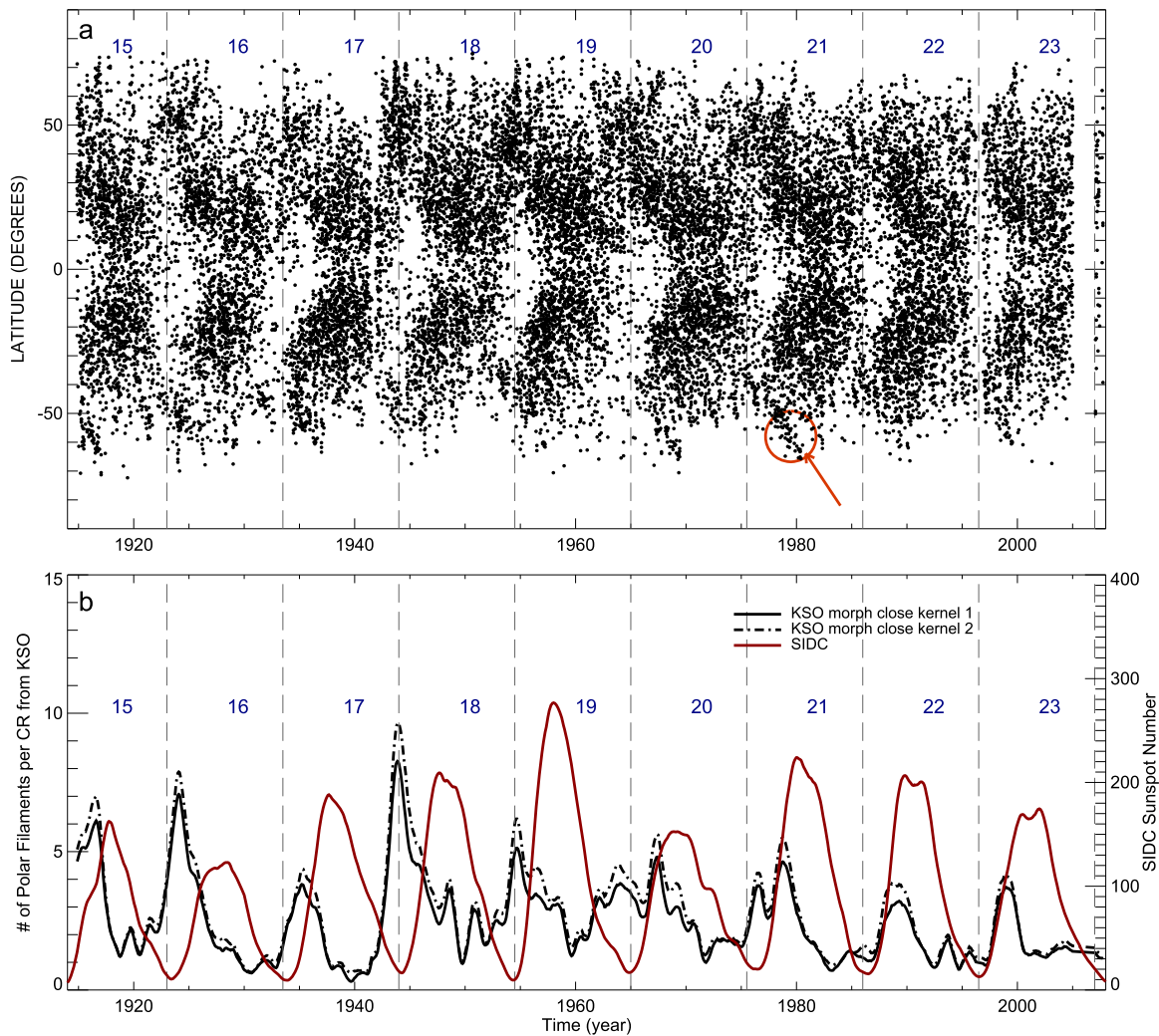
**Figure 7.** Distribution of filaments. (a) Time-latitude distribution (1914–2007) of solar filaments as detected from KSO Carrington maps. A representative signature of poleward migration is marked by a red circle and an arrow. Cycle numbers are printed in blue with dashed vertical lines marking the cycle minima. (b) Temporal variation (1914–2007) of the number of polar filaments as recorded from KSO and its comparison with the SIDC sunspot number. The solid black curve and dotted–dashed curve correspond to the filaments morphologically closed by a disk kernel of with a radius of 22 pixels and 30 pixels, respectively. It is worth noting that the temporal locations of the filament number maxima do not change with the different sizes of the closing operation kernel, except for the relative change in the number of filaments.
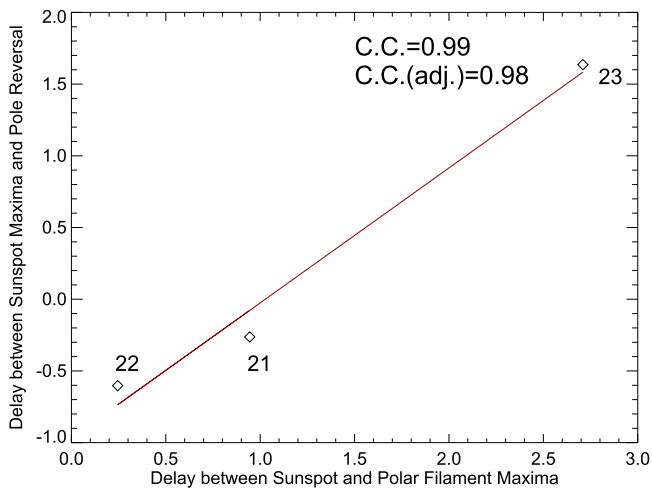


**Figure 8.** Correlation of the sunspot-polar filament number maxima delay and sunspot number maxima-pole reversal delay for the last three cycles. As the number of data points is only three, the adjusted correlation coefficient is also shown.

Wilcox Solar Observatory data for the last three cycles. These have been used to correlate the sunspot number-polar filament delay and sunspot number-pole reversal delay. With limited study points, we found very high correlation, indicating the role of polar filaments in polar reversal. This new result, along with the rate of drift of filaments toward the pole, may shed new light on polar reversal.

3. We found asymmetry in the histogram of filament tilts consistent with the finding of Tlatov et al. (2016b). Also, we observed behavior similar to Joy's law in the latitudinal distribution of the filament tilts. It is believed that the tilt angle of sunspots and bipolar groups determines the conversion efficiency of the toroidal field into the poloidal magnetic field (Tlatov et al. 2016b). As filaments lie along polarity inversion lines, measurements of their tilt angle help us understand the distribution of the solar magnetic field across the solar disk. In contrast to sunspots, filaments are distributed at all latitudes, so the long-term variation of the distribution of the poloidal and toroidal components of magnetic fields may be better studied if we follow the filament distribution.
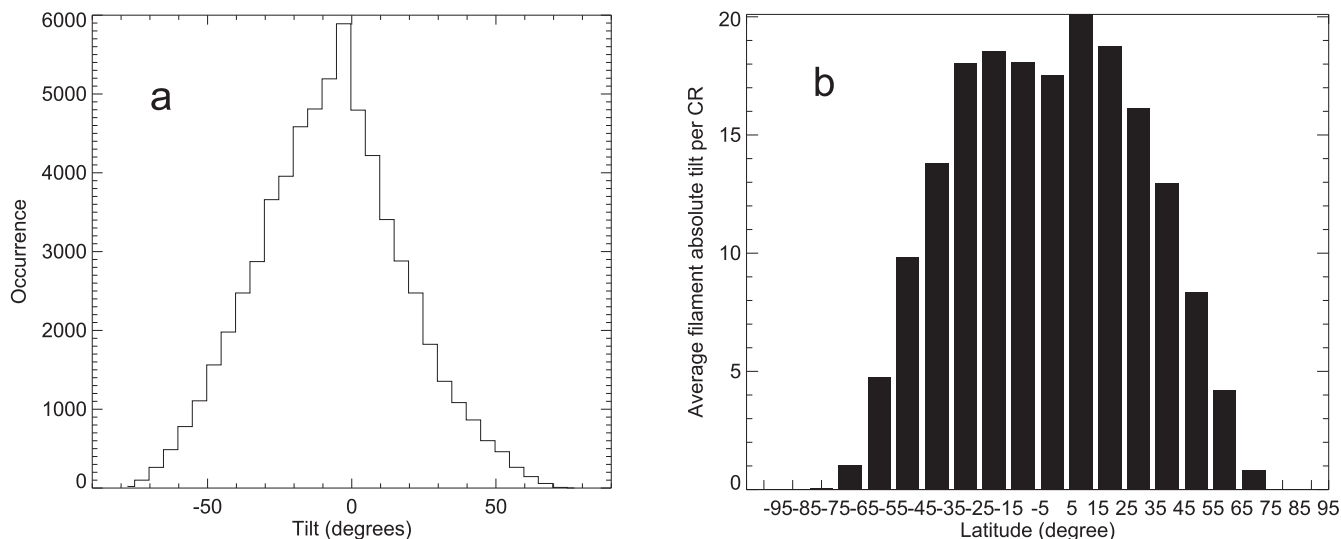
**Figure** Filament tilt attributes. (a) A histogram of the filament tilt angle with respect to the equator and (b) the latitudinal distribution of the solar filament tilts.

In this paper we announce the availability of the largest digitized archive of the H$_\alpha$ data set (1914–2007) from the Kodaikanal Solar Observatory. The data will be made public through its portal at http://kso.iiap.res.in/data. We also show representative results from this archive to prove the potential of such an archive, which demands further detailed investigations. In our subsequent studies on filaments, we want to combine a multiwavelength analysis of the historical data from KSO as hinted in this paper. This can lead to the classification of filaments into active region filaments, and quiescent filaments. We also want to explore the hemispheric differences in filament behaviors and find more proxies to predict future cycles. As a next step, we will employ different techniques for eliminating filament fragmentation in order to estimate the filament lengths correctly. The length determination may prove to be vital in terms of its correlation to different statistical studies related to filament eruption and CMEs (Filippov & Koutchmy 2008; Ruzmaikin et al. 2011). We plan to carry out a work similar to Ipson et al. (2005) that will include magnetic neutral line detection from the MDI Carrington maps and cross-calibration with KSO filament maps of intersecting dates to predict polar inversion line locations in the past. We hope that this KSO archive and some of the new results presented here will provide new momentum for the long-term study of H$_\alpha$.

## ORCID iDs

Subhamoy Chatterjee ⓘ https://orcid.org/0000-0002-5014-7022
Dipankar Banerjee ⓘ https://orcid.org/0000-0003-4653-6823

## References

Ananthakrishnan, R. 1952, Natur, 170, 156
Bonnin, X., Aboudarham, J., Fuller, N., Csillaghy, A., & Bentley, R. 2013, SoPh, 283, 49
Chatterjee, S., Banerjee, D., & Ravindra, B. 2016, ApJ, 827, 87
Chen, P. F., Innes, D. E., & Solanki, S. K. 2008, A&A, 484, 487
Evershed, J. 1907, MNRAS, 67, 477
Evershed, J. 1908, MNRAS, 68, 515
Filippov, B., & Koutchmy, S. 2008, AnGeo, 26, 3025
Gilbert, H. R., Holzer, T. E., Burkepile, J. T., & Hundhausen, A. J. 2000, ApJ, 537, 503
Gopalswamy, N., Hanaoka, Y., & Hudson, H. S. 2000, AdSpR, 25, 1851
Gopalswamy, N., Shimojo, M., Lu, W., et al. 2003, ApJ, 586, 562
Hao, Q., Fang, C., Cao, W., & Chen, P. F. 2015, ApJS, 221, 33
Ipson, S. S., Zharkova, V. V., Zharkov, S., et al. 2005, SoPh, 228, 399
Li, K. J. 2010, MNRAS, 405, 1040
Li, K. J., Li, Q. X., Gao, P. X., et al. 2007, JApA, 28, 147
Low, B. C. 1982, RvGeo, 20, 145
Makarov, V. I., & Sivaraman, K. R. 1983, SoPh, 85, 227
Martin, S. F. 1998, SoPh, 182, 107
McIntosh, P. S. 1972, RvGSP, 10, 837
Mouradian, Z., & Soru-Escaut, I. 1994, A&A, 290, 279
Rausaria, R. R., Gupta, S. S., Selvendran, R., Sundara Raman, K., & Singh, J. 1993a, SoPh, 146, 259
Rausaria, R. R., Sundara Raman, K., Aleem, P. S. M., & Singh, J. 1993b, SoPh, 146, 137
Ruzmaikin, A., Feynman, J., & Stoev, S. A. 2011, JGRA, 116, A04220
Sheeley, N. R., Jr., Cooper, T. J., & Anderson, J. R. L. 2011, ApJ, 730, 51
Sonka, M., Hlavac, V., & Boyle, R. 2014, Image Processing, Analysis, and Machine Vision (4th ed.; Stamford, CT: Cengage Learning)
Sundara Raman, K., Aleem, S. M., Singh, J., Selvendran, R., & Thiagarajan, R. 1994, SoPh, 149, 119
Sundara Raman, K., Ramesh, K. B., & Selvendran, R. 2001, BASI, 29, 77
Tlatov, A. G., Kuzanyan, K. M., & Vasil'yeva, V. V. 2016a, in ASP Conf. Ser. 504, Coimbra Solar Physics Meeting: Ground-based Solar Observations in the Space Instrumentation Era, ed. I. Dorotovic, C. E. Fischer, & M. Temmer (San Francisco, CA: ASP), 241
Tlatov, A. G., Kuzanyan, K. M., & Vasil'yeva, V. V. 2016b, SoPh, 291, 1115
Zhang, Q. M., Chen, P. F., Xia, C., & Keppens, R. 2012, A&A, 542, A52
Zharkova, V., Ipson, S., Benkhalil, A., & Zharkov, S. 2005, Artif. Intell. Rev., 23, 209
Zharkova, V. V., & Schetinin, V. 2003, in A Neural-Network Technique for Recognition of Filaments in Solar Images, ed. V. Palade, R. J. Howlett, & L. Jain (Berlin: Springer), 148